Available online at www.sciencedirect.com
SCIENCE DIRECT
Earth and Planetary Science Letters 235 (2005) 244–260
EPSL
www.elsevier.com/locate/epsl

U–Pb zircon ages as a sediment mixing tracer in the Nepal Himalaya

William H. Amidon[a,*], Douglas W. Burbank[a], George E. Gehrels[b]

[a]Department of Geological Sciences, University of California Santa Barbara, Santa Barbara, CA 93106, United States
[b]Department of Geosciences, 1040 E. 4th Street, University of Arizona, Tucson, AZ 85721, United States

Received 14 September 2004; received in revised form 13 March 2005; accepted 18 March 2005
Available online 26 May 2005
Editor: K. Farley

Abstract

This paper presents a new approach to quantify sediment mixing based on the mixing of U–Pb zircon age distributions within sediment. Two statistical techniques are presented to determine the proportion in which two known age distributions combine to create a known mixed age distribution. These techniques are then used to determine relative erosion rates between adjacent drainage basins above and below the Main Central Thrust (MCT) in the central Nepal Himalaya. The MCT region is coincident with an abrupt north–south change in geomorphic character and mineral cooling ages that are thought to represent an erosional response to higher rock uplift rates north of the MCT zone. However, it is unclear whether the ongoing deformation responsible for the differential uplift rates is: (1) focused on the MCT; (2) at depth along a crustal scale ramp; or (3) along newly mapped thrust faults south of the MCT. Our study explores this issue by comparing modern erosion rates with longer-term erosion rates determined from mineral cooling ages. Zircons were separated from modern river sand and dated by LA-MC-ICPMS before the measured isotopic ratios and ages were used in 1-d and 2-d mixing calculations. The 1-d technique creates probability density functions of zircon ages for each sample and then uses both an iterative and inverse approach to estimate mixing between samples. In contrast, the 2-d technique estimates mixing between probability "fields" defined by the measured $^{238}U/^{206}Pb$ and $^{207}Pb/^{206}Pb$ ratios. Given a finite mixture with perfect sample representation, both techniques produce perfect mixing estimates across a range of mixing proportions. Modeling results demonstrate that given imperfect subsample representation of the complex parent age distribution, differing degrees of subsample smoothing may be required to achieve an accurate mixing estimate. Using mixing of zircon ages as a quantitative proxy for sediment mixing requires a correction for the concentration of zircon in the river sediment. Two new methods for establishing zircon concentration in river sediment are presented demonstrating the existence of 2- to 5-fold differences in zircon concentration between adjacent drainages. Relative erosion rates are estimated by determining the zircon mixing ratio between adjacent drainages which are then normalized by the ratio of zircon concentrations and the ratio of drainage areas. Results show ~3 times higher modern erosion rates south of the

* Corresponding author. Tel.: +1 805 893 7242, fax: +1 805 893 2314.
E-mail addresses: willyamidon@umail.ucsb.edu (W.H. Amidon), burbank@crustal.ucsb.edu (D.W. Burbank), ggehrels@geo.arizona.edu (G.E. Gehrels).

0012-821X/$ - see front matter
doi:10.1016/j.epsl.2005.03.019

MCT in the northernmost Lesser Himalaya. Future applications of this new technique may include reach-scale sediment transport dynamics, improved sedimentary basin analysis, and better interpretation of foreland mineral cooling ages.

Keywords: sediment mixing; U–Pb; detrital; zircon; Himalaya; Nepal; erosion; provenance

1. Introduction

The primary goal of this paper is to present a new technique using mixing of U–Pb zircon ages to evaluate sediment mixing between multiple sources. This technique is then used to measure relative erosion rates between adjacent drainage basins in the Nepal Himalaya where considerable debate exists over erosion rates on both modern and geologic timescales. This approach fills a unique niche in its ability to fingerprint individual sediment populations and quantitatively address mixing and erosional fluxes in the fluvial system. Previous methods applied to similar problems include heavy mineral point counting, sediment geochemistry, and identification of age peaks in detrital geochronological data. Point counting is tedious, and often limited by overlapping source areas for a given mineral, significant uncertainties in mineral abundances, and selective destruction of certain minerals [1,2]. Sediment geochemistry is often limited by the overlap of isotopic signatures, as well as by chemical alteration of sediments [3,4]. Identification of age peaks in distributions of single grain detrital geochronological ages is used to constrain potential source terranes but rarely to trace sediment in the modern fluvial system [5–8]. The two techniques presented here have the potential to provide rapid, inexpensive, unambiguous estimates of sediment mixing that can be applied to problems in fields ranging from geomorphology to sedimentology and paleotectonics.

The first approach creates a probability density function (PDF) of U–Pb ages from each sample and uses both an iterative and an inverse approach to determine in what proportion the two constituent PDFs combined to create the mixed PDF. The second approach uses two-dimensional iterative and inverse analyses in which the simultaneously measured $^{238}U/^{206}Pb$ and $^{207}Pb/^{206}Pb$ ratios define probability "fields" for each sample. Modeling results show the importance of sample size, complexity, and smoothing in obtaining an accurate mixing calculation.

Motivated by the ongoing debate over modern rock uplift near the Main Central Thrust (MCT) zone in central Nepal, we use the mixing techniques to calculate relative erosion rates in drainages above and below the MCT [9–14]. Once the proportion of zircons (zirc) derived from each of the two upstream drainages (A and B) is known, relative erosion rates (RER) are determined by correcting for the relative concentrations (conc) of zircon in the river sediments and the relative drainage areas (Eq. (1)).

$$\mathrm{RER}_{A/B} = A_{\mathrm{zirc}}/B_{\mathrm{zirc}} * B_{\mathrm{conc}}/A_{\mathrm{conc}} * B_{\mathrm{area}}/A_{\mathrm{area.}} \quad (1)$$

Results from both sites show ~3 times higher modern erosion rates in the northernmost Lesser Himaalaya just south of the MCT.

2. Tectonic history and geomorphology of the central Nepal Himalaya

The meta-sedimentary rocks of the Nepal Himalaya are broadly grouped into three units: the mainly Proterozoic Lesser Himalayan Series; the late Proterozoic–early Cambrian Greater Himalayan Series; and the Paleozoic–Mesozoic Tethyan Sedimentary Series [15] (Figs. 1 and 2). These units are generally thought to represent different proximal-to-distal depositional environments on the passive Indian margin [8,16]. In central Nepal, the units also represent distinct depositional periods as reflected by Lesser Himalayan U–Pb zircon ages exclusively older than ~1500 My, contrasting with Greater Himalayan ages between ~600 and 3300 My [16,17].

The classically defined MCT zone is a 1–3-km-thick zone of north-dipping, sheared and faulted rocks juxtaposing amphibolite grade Lesser Himalayan rocks in its footwall with the gneisses of the Greater Himalaya in its hanging wall (Fig. 2). Recent work from central Nepal suggests that the MCT can be precisely defined on the northern margin of the

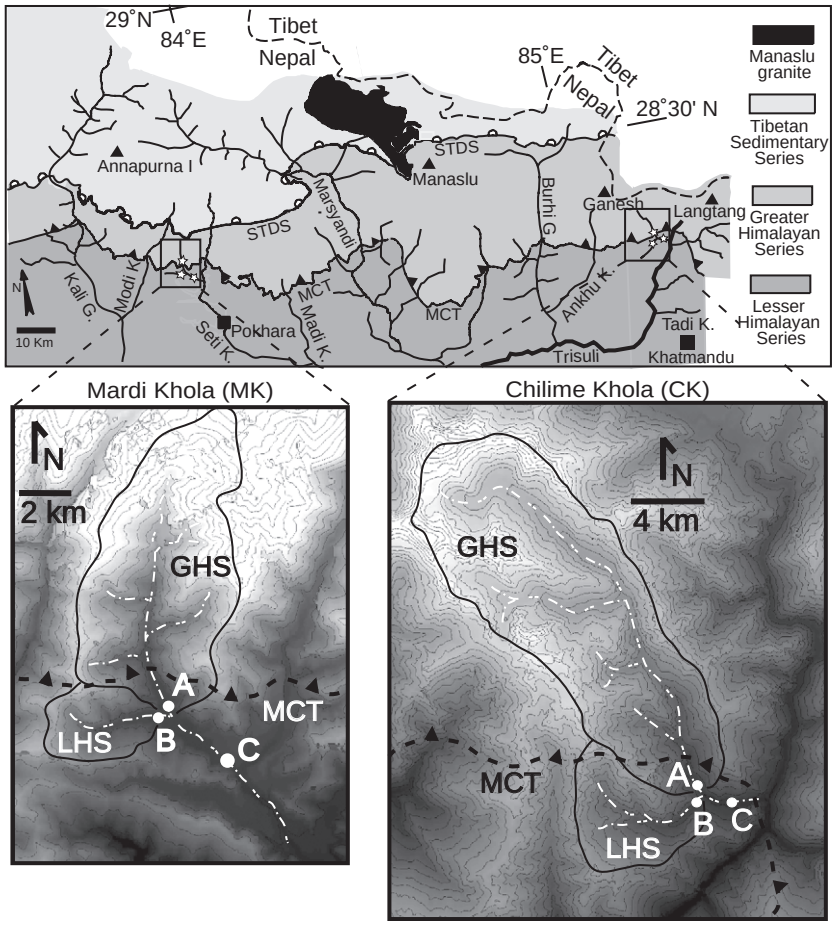

Fig. 1. Generalized geologic map of central Nepal, modified after [38]. Field sites are shown as shaded contoured maps derived from a 3 arc-second digital elevation model. Approximate location of the MCT is defined by field observations and published maps [39–41].

deformed zone, and that deformation to the south occurs along structurally lower thrust faults entirely within Lesser Himalayan rocks [10,17,18]. In this study we define the MCT as the northernmost boundary between rocks of definitively Greater Himalayan and probable Lesser Himalayan affinity as mapped by [39–41]. In most reconstructions, the MCT is thought to have initiated in the early Miocene and become inactive by ~10 Ma, when deformation stepped southward toward the foreland along the Main Boundary Thrust, and eventually onto the Main Frontal Thrust [19,20]. Modern geodetic and geologic data suggest that the central Nepal Himalaya are currently experiencing ~20 mm/yr of orogen-perpendicular shortening, all of which can be accounted for along the southernmost Main Frontal Thrust during the past 10 ky [21–23].

Recent geomorphic, structural, and thermochronologic evidence contradict this interpretation, suggesting that Plio-Pleistocene deformation has taken place near the MCT zone. This idea was first proposed by Seeber and Gornitz [24], who noted that abrupt drops in transverse river gradients from north to south across the Himalayan front define a laterally continuous transition in geomorphic character. Noting the coincidence of this transition with a band of moderate magnitude earthquakes, and the trace of the MCT, they proposed ongoing deformation near a “basement thrust front” as the underlying cause. Inherent in this model is the idea that a significant break in rock uplift

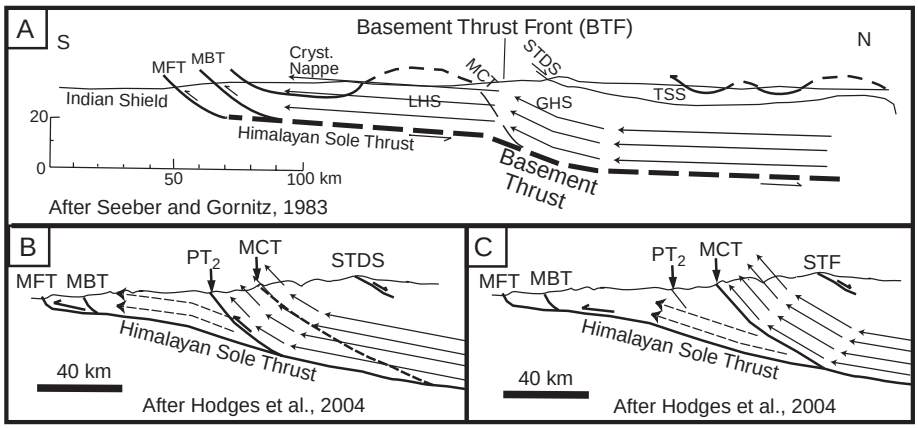

Fig. 2. Cartoon cross-sections showing three different models for differential rock uplift rates near the MCT. (A) Cross-section modified from Seeber and Gornitz [24] showing the possibility of broadly distributed uplift along a crustal scale ramp. (B) Cross-section modified from Hodges et al. [10] illustrating uplift along a previously unmapped thrust fault near the PT_2. (C) Similar cross-section to B, but illustrating the differential rock uplift that would result from reactivation of the MCT. Models A and B have been proposed to explain the break in geomorphic character and cooling ages associated with the PT_2.

rate occurs near the MCT. This idea has been supported by observations that the originally defined north to south transition is also roughly coincident with: (1) an abrupt transition from gorge-contained river to an open alluvial valley [9,25]; (2) a distinct drop in mean hillslope angle [9,25,26]; (3) a drop in channel steepness index (k_s) [9,10]; and (4) a ~4-fold drop in Holocene river incision rates [25]. In central Nepal, these transitions do not coincide with the MCT, but occur 3–15 km south of the fault trace at a transitional boundary dubbed the physiographic transition 2 (PT_2) [27]. The disconnect between the apparent focus of differential uplift and the location of the MCT has led to a discussion about the driving mechanism for Plio-Pleistocene uplift. The three most common ideas are: (1) reactivation of the MCT; (2) broad uplift above a crustal-scale ramp; and (3) deformation along previously unmapped structures 3–15 km south of the MCT (Fig. 2). The first idea is supported by syn-deformational muscovite $^{40}Ar/^{39}Ar$ ages of Pliocene age from a shear fabric within the MCT that has been overprinted with brittle deformation as recently as the Pleistocene [10]. The second idea is largely based on seismic constraints and inferred structural geometries based on the assumption that the MCT has remained inactive since the early Miocene [28]. The third idea is supported by spatial agreement between the observed geomorphic evidence and the existence of newly mapped thrust faults south of the MCT [10]. Deformation on one of these faults, the Nadi, is constrained by syn-deformational muscovite $^{40}Ar/^{39}Ar$ ages of Pliocene age [10]. Additionally, Pliocene activity is supported by the existence of peak metamorphic conditions below the fault at 8.1–3.3 Ma compared with ~18 Ma above the fault [10,29].

Mineral cooling ages also provide evidence for breaks in exhumation rate in the MCT region. The first hypothesis is supported by a transect of apatite fission-track ages along the Marsyandi river that fluctuate around a mean age of 0.5 ± 0.2 My throughout the Greater Himalaya before increasing abruptly to an age of ~2 My immediately south of the MCT, and to ~4 My further south [30] (Fig. 3). These data suggest that the major break in erosion rate over the last 2 My has been focused across the MCT rather than the PT_2. In contrast, detrital muscovite $^{40}Ar/^{39}Ar$ ages from the Burhi Gandaki river show consistent late Miocene–Pliocene ages across the MCT abruptly increasing to Paleozoic and older ages south of the PT_2 [9] (Fig. 3). Similarly, muscovite $^{40}Ar/^{39}Ar$ ages along the Ankhu River show consistently late Miocene and Pliocene ages across the MCT abruptly increasing to Mesozoic ages 20–25 km SSW of the MCT [29]. These data strongly support the idea that the break in long-term exhumation rates occurs in conjunction with the PT_2, possibly in response to deformation along recently mapped thrust faults within the Lesser Himalaya.

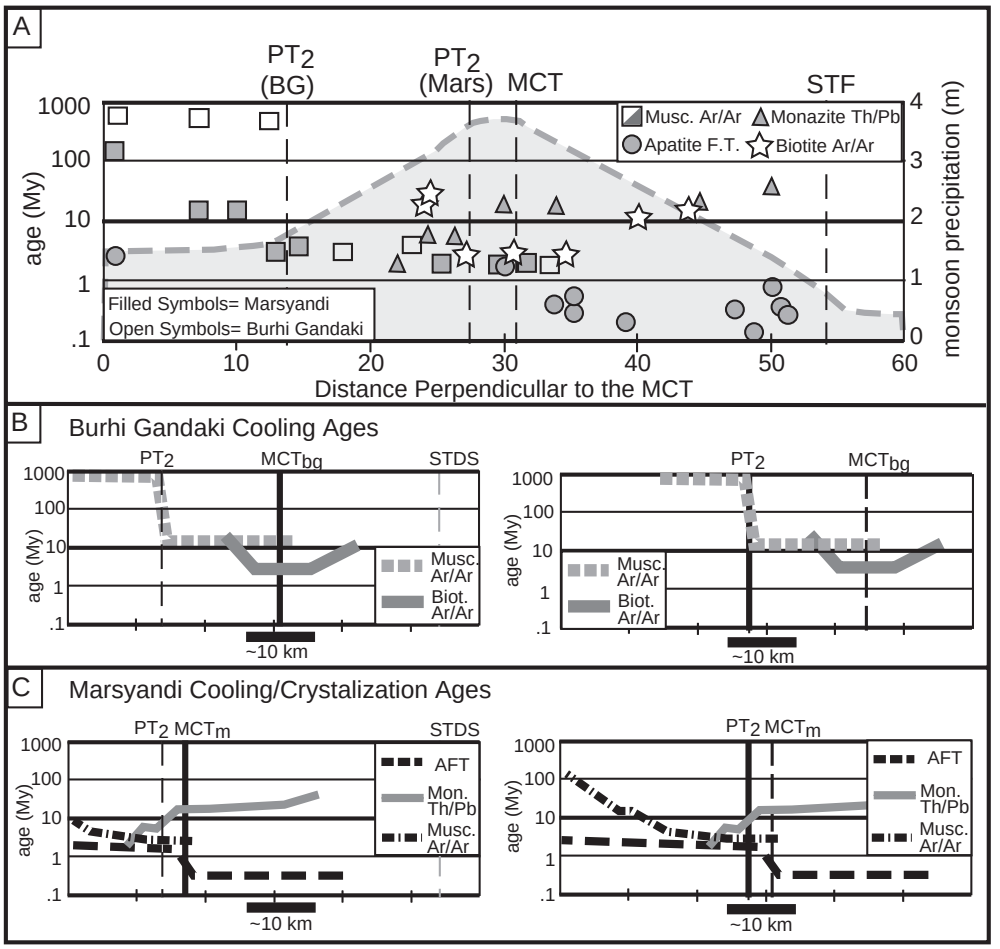

Fig. 3. (A) Published mineral cooling ages from central Nepal plotted with relation to the generalized locations of the MCT and PT_2 in the Burhi Gandaki (BG) and Marsyandi (Mars) drainages. Open symbols represent data from the Burhi Gandaki drainage, whereas filled symbols represent data from the Marsyandi drainage. Open squares are $^{40}Ar/^{39}Ar$ muscovite ages from Wobus et al. [9], open stars are $^{40}Ar/^{39}Ar$ biotite ages from Copeland et al. [14]. Filled squares are $^{40}Ar/^{39}Ar$ muscovite ages from Catlos et al. [29], filled circles are apatite fission-track ages from Burbank et al. [30], filled hexagons are U–Pb monazite ages reported in Catlos et al. [29]. The heavy dashed line and shaded area shows monsoonal precipitation as reported in [30]. (B) Generalized trends in mineral ages aligned with respect to the MCT (left) and PT_2 (right) in the Burhi Gandaki drainage. Dashed lines represent detrital $^{40}Ar/^{39}Ar$ muscovite ages from tributary catchments [9], solid lines represent $^{40}Ar/^{39}Ar$ biotite ages from bedrock [14]. (C) Generalized trends in mineral ages aligned with respect to the MCT (left) and PT_2 (right) in the Marsyandi drainage. Dashed lines represent apatite fission-track ages [30], dash-dot lines represent muscovite $^{40}Ar/^{39}Ar$ ages [29], and solid lines represent U–Pb monazite ages [29]. Whereas fission-track and $^{40}Ar/^{39}Ar$ ages are interpreted as a proxy for exhumation rate, U–Pb monazite ages are interpreted to represent the timing of peak metamorphic conditions.

The break in $^{40}Ar/^{39}Ar$ cooling ages in the Lesser Himalaya corresponds spatially with the peak in monsoonal precipitation [9] (Fig. 3a). Supported by numerical modeling results, focused orographic precipitation has been proposed to drive rapid erosion and structural unloading, promoting recent deformation [9,27,31,32]. Although this idea is supported by $^{40}Ar/^{39}Ar$ ages, the transect of apatite fission-track ages seemingly refutes it and suggests that climate is not exerting a first order control on erosion rate because: (1) the youngest fission-track ages are not spatially coincident with the peak in monsoonal precipitation; and (2) ages are constant throughout the Greater Himalaya despite a strong precipitation gradient [30]. This is paradoxical because the fission-track ages record exhumation over much more recent

timescales than the $^{40}Ar/^{39}Ar$ ages and thus would be expected to show a stronger correlation with the modern precipitation gradient.

By measuring relative erosion rates above and below the MCT, our study permits comparison of modern erosion rates with longer term exhumation rates. If our results are consistent with the fission-track transect, showing higher erosion rates above the MCT, this would suggest that modern erosion rates are being driven by higher rates of rock uplift in the Greater Himalaya, north of the MCT. In contrast, if rock uplift is focused south of the MCT near the PT_2, then the highest rates should occur near the peak in monsoonal precipitation in the northernmost Lesser Himalaya.

3. Field and laboratory methods

3.1. Field methods

Relative erosion rates were determined for two sites in the Nepal Himalaya: the Chilime Khola which drains the eastern side of Ganesh Himal; and the Mardi Khola, rising on the southern flanks of Machupucharre (Fig. 1). Each site consists of adjoining drainages deriving sediment primarily from either Greater or Lesser Himalayan rocks. Coarse-very coarse (500–2000 μm) sand samples were taken from the trunk stream where it emerged from above the MCT having drained entirely Greater Himalayan rocks (sample A), from the mouth of an adjoining tributary draining exclusively Lesser Himalaya (sample B), and from the trunk stream 2–3 km below the confluence of A and B (sample C). Throughout the text, A, B, and C will refer to the Greater Himalayan, Lesser Himalayan, and mixed sample, respectively.

3.2. Laboratory methods

3.2.1. Zircon dating

All zircons were separated using consistent heavy liquid and magnetic separation before a random sub-population was selected for analysis. The isotopes ^{238}U, ^{232}Th, ^{208}Pb, ^{207}Pb, ^{206}Pb, ^{204}Pb were measured simultaneously by laser-ablation multi-collector, inductively coupled plasma-mass spectrometry (LA-MC-ICPMS) [33], and separate ages were calculated from the ratios $^{238}U/^{206}Pb$, $^{235}U/^{207}Pb$ and $^{207}Pb/^{206}Pb$. Use of a laser-ablation system is critical to this technique because it allows rapid analysis of many grains and offers the possibility of randomly analyzing grains, rather than handpicking them. Individual grains were randomly chosen for analysis by moving along a grid and analyzing the five closest zircons to each grid point that were large enough (>50 μm width) and of adequate quality for analysis. Heavily fractured or metamict zircons were not analyzed.

3.2.2. Establishing zircon concentration in modern river sediment

Before using the mixing of zircon ages as a proxy for sediment mixing, a correction must be applied for the relative concentration of zircon in the sediment of each contributing source. Relative concentrations of zircon were estimated using two techniques: (1) zirconium concentrations (ppm Zr) determined by XRF analysis;

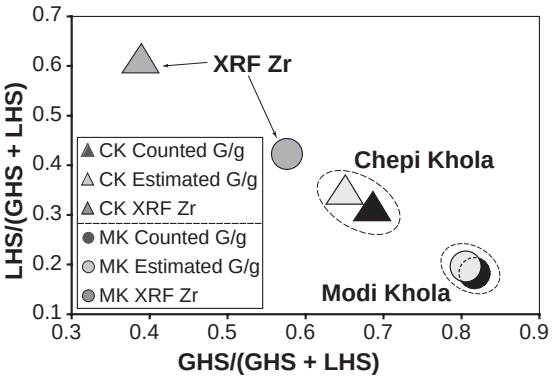

Fig. 4. Normalized zircon concentrations for the Chilime Khola and Mardi Khola determined by each of the three techniques discussed in the text: bulk Zr concentration measured by XRF; grains/gram concentration measured by grain counting; and estimated grains/gram concentration. Unitless values on the *x*-axis are attained by dividing the Greater Himalayan concentration by the combined Greater and Lesser Himalayan concentrations for a given technique at a given field site. Bulk Zr concentrations determined by XRF do not match the grains/gram concentration determined by grain counting, because Zr concentration is a function not only of zircon concentration, but also of grain size and morphology. Using grain size and morphology distributions for each sample, a grains/gram concentration was estimated from the Zr concentration as shown in Fig. 5. The close match between the counted and estimated grains/gram concentrations suggests that: (1) concentrations have been accurately determined; and (2) Zr concentration can be used as a proxy for zircon concentration if the distribution of grain size and morphologies are known.

and (2) the number of zircon grains per gram of sediment determined by grain counting. Bulk Zr concentration is a good proxy for zircon concentration because zircon is the only mineral present that contains significant amounts of Zr. Grain counting was performed by sieving the bulk sand sample, separating, photographing and counting all zircons >50 μm in width.

Initial results show poor agreement between the two techniques (Table 1 online; Fig. 4). This is because grain counting is sensitive only to the absolute number of >50 μm zircons in the sample, while bulk Zr is sensitive to grain volume, which is a function of grain abundance, size, and morphology. Because our zircon mixing calculations use one U–Pb age for each zircon regardless of grain volume, we must use the concentrations determined by grain counting to characterize the ratio B_{conc}/A_{conc} (Eq. (1)). However, a grains/gram concentration can be estimated from a bulk Zr concentration and is useful as: (1) an independent check on the reliability of our grain-counting estimate and (2) a way to estimate grains/gram without exhaustive grain-counting campaigns. To estimate grains/gram from bulk Zr, the average zircon-grain volume in each sample must be determined. Our strategy was to define categories of geometric grain shapes, measure photogrametrically the grain abundance and mean volume of each shape, calculate the average zircon-grain volume, and finally, the average Zr per grain. The average Zr per grain is then divided by the total Zr in the sample to yield an estimate of the total number of zircons in the sample (Fig. 5).

The results show agreement within ±10% between the counted grains/gram concentration and the grains/gram concentration estimated from the bulk Zr data (Table 1 online; Fig. 4). This agreement suggests that both concentration estimates are fairly accurate and that bulk Zr can be used to estimate the concentration of zircon if the distribution of grain size and morphology are known for the sample.

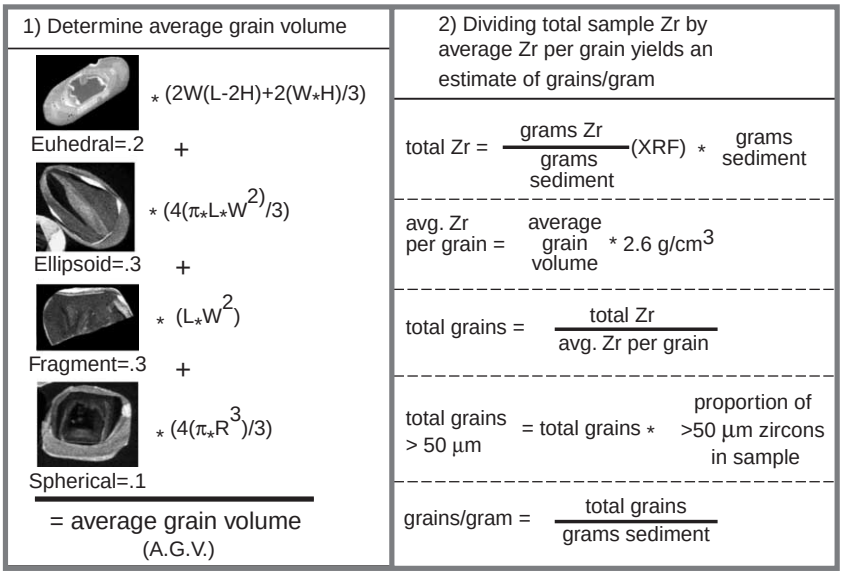

Fig. 5. Technique used to estimate the number of zircon grains per gram of sediment using the bulk Zr concentration measured by XRF. Step 1: photograph all zircons and determine the proportion and average length and width of each of four morphologic categories. Calculate average grain volumes for each category using the average length and width assuming that: (1) the A and B crystallographic axes are of equal length for all morphologies; (2) euhedral grains are defined by a cuboid body capped on either end by a pyramid such that $h = b/8$; (3) grain fragments are approximated by a cuboid. Calculate overall average grain volume for the sample by multiplying the observed proportion of each morphology by its average grain volume. Step 2: determine total mass of Zr in the sample by multiplying the ppm Zr (measured by XRF) by total sample mass, then dividing by the average mass of Zr per grain to yield the total number of zircon grains in the sample. Multiplying by the observed proportion of >50μm grains in the sample yields a final estimate of >50μm grains in the sample, which can be divided by sample mass for an estimate of datable zircon concentration in units of grains/gram.

4. 1-D mixing of U–Pb zircon ages using PDFs

4.1. Construction of PDFs

We define a PDF as a normalized combination of measured grain ages and their associated Gaussian errors.

$$\mathrm{PDF} = \sum_{i=1}^{N} \left(1/2\sigma_i\sqrt{2\pi}\right) \mathrm{e}^{-(x-\mu_i)^2/2\sigma_i^2}. \quad (2)$$

In this study, $^{238}U/^{206}Pb$ ages are used for grains with an average age of <1 Gy, whereas $^{207}Pb/^{206}Pb$ ages are used for average ages >1 Gy. Ages with >20% error, >20% normal discordance, or >10% reverse discordance were not included in sample PDFs. In all cases, 1σ errors are used, typically between 4% and 10%, which include measurement error, ^{204}Pb correction error, and fractionation correction error.

4.2. Smoothing of subsample PDFs

Whereas one goal of detrital age studies is an accurate characterization of the actual (or "parent") frequency distribution of ages in a catchment, researchers are commonly limited to a subsample from which a finite number (~100) of ages are determined. Given the broad spectrum of observed Himalayan ages (0.02–3.5 Ga) and the relatively small errors associated with individual ages, resultant age PDFs are commonly "spiky" and not well matched with the parent. Better matches between the parent and subsample can be obtained by comparing smoothed PDFs. Such smoothing can be justified for complex detrital PDFs given the experimental observation that larger numbers of ages (400 versus 100) almost always yield a less spiky, more closely matched PDF. Moreover, field studies show that multiple ages from a restricted area of bedrock typically yield an age range that significantly exceeds the uncertainty on any individual date. In detrital dating, however, only a few grains are likely to be drawn from that bedrock area. Hence, smoothing of the resulting PDF will more completely represent the actual abundance of ages.

To determine the degree of smoothing that would make a sampled PDF best approximate the parent population, we created two artificial parent PDFs each consisting of between 400 and 500 Himalayan zircon ages derived from either the Greater or Lesser Himalaya [16]. A series of experiments were run in which Monte-Carlo subsampling defined 100 grain subsamples from the parent populations. Each sampled age was assigned an average error based on the errors of the parent population. A subsampled PDF was created and then smoothed using successively larger smoothing windows from 0 to 200 Ma, with the mismatch between parent and subsample calculated for each smoothing interval. 100 trials were repeated and averaged for each parent population, until the smoothing window that gave the best match between parent and subsample was determined for each parent population. Parent and sample PDFs were compared by calculating areal percent mismatch (Eq. (3)), as well as the Kolmogorov–Smirnov statistic [34].

$$\left(\left(\sum_{i=1}^{N} |\mathrm{parent} - \mathrm{daughter}|\right)\Big/2\right) \times 100. \quad (3)$$

The average percent mismatches for each smoothing window (Fig. 6) show that the Lesser Himalayan distribution achieved the lowest mismatch (~12%) between the parent and subsample at around 50 My, whereas the Greater Himalayan distribution yielded a minimum mismatch of only ~17% at around 80 My. In general, smoothing has a more significant effect on reducing mismatch for the Greater Himalayan distribution, and does not greatly reduce the mismatch of the Lesser Himalayan sample. Additionally, the Lesser Himalayan PDF required considerably less smoothing to achieve the optimal mismatch and excessive smoothing causes a significant increase in mismatch. This contrast with the Greater Himalayan sample results from the smaller range of ages and more condensed probability distribution of the Lesser Himalayan distribution (Fig. 6A). This experiment confirms that the optimal degree of subsample smoothing is a function of the parent PDF complexity and that smoothing is more important for more complex distributions.

4.3. Mixing of PDFs

The proportion in which two upstream samples (A and B) mixed to create the downstream sample C can be

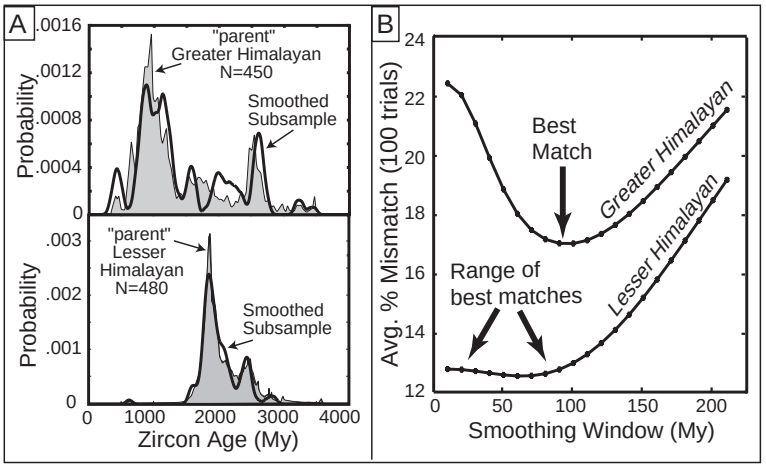

Fig. 6. (A) PDFs of the artificially created parent age distributions and 100 grain subsamples drawn from each. The Greater Himalayan and Lesser Himalayan subsampled PDFs have been smoothed to 80 and 30 My, respectively, to achieve the optimal match between the parent and subsample PDFs. (B) Modeling results showing the percent mismatch between parent and subsample for a given smoothing window averaged over 100 trials. The more complex Greater Himalayan distribution is more sensitive to smoothing and requires a larger smoothing window to achieve the optimal parent-subsample match. The simpler Lesser Himalayan distribution is less sensitive to smoothing and shows an optimal match over a range of smoothing windows between 30 and 60 My.

determined by either an iterative or inverse approach. The basis for both approaches is the statement that:

$$\phi P(A) + (1-\phi)P(B) = P(C) \tag{4}$$

where $P(A,B,C)$ are the PDFs representing each sample and ϕ is a proportionality term such that $0<\phi<1$. ϕ literally represents the proportion of $P(A)$ present in the mixed $P(C)$. Assumptions implicit in Eq. (4) are that: (1) sample C is a "finite mixture" composed only of contributions from A and B; and (2) the smoothed sample PDFs accurately represent the parent distribution of each sample. If these fundamental assumptions are satisfied, then a single ϕ value will satisfy Eq. (4) at every age increment (i) of the PDFs. In reality, because no subsample will exactly replicate the parent PDF, the second assumption is usually violated, and the equality does not hold true at every age increment. In this section, we present two techniques to determine the ϕ value that best defines mixing between imperfectly defined PDFs.

4.3.1. The inverse approach to PDF mixing

A least-squares inversion can be applied to estimate the value of ϕ by rewriting Eq. (4) in the form $Ax=B$:

$$[P(A)-P(B)]\phi = [P(C)-P(B)] \tag{5}$$

where A is a column vector consisting of the values of $[P(A)-P(B)]$ at every age increment (i), x is the unknown parameter ϕ, and B is a column vector consisting of the values of $[P(C)-P(B)]$ at every age increment.

In effect, a least-squares inversion will determine the single ϕ that minimizes the sum of the squared difference between the two sides of Eq. (5) at every increment (i) (Fig. 5). Following Menke [35], this ϕ value can be estimated by:

$$\phi_{\text{est}} = \left[A^T A\right]^{-1} A^T B. \tag{6}$$

4.3.2. The iterative approach to PDF mixing

Mixing between age PDFs can be assessed iteratively by combining $P(A)$ and $P(B)$ for every possible ϕ until the resulting mixed $P(C)_{\text{predicted}}$ has the lowest mismatch with $P(C)_{\text{observed}}$. PDFs are combined by multiplying all probability values in A and B by ϕ or $(1-\phi)$, respectively, then adding the two distributions to create $P(C)_{\text{predicted}}$ (see Fig. 1 online). We attempted to solve for ϕ by minimizing either the Kolmogorov–Smirnov statistic or percent mismatch. Minimizing the Kolmogorov–Smirnov statistic was ineffective because it is insufficiently sensitive to small differences between PDFs; thus, all iterative

results presented here were achieved by minimizing percent mismatch.

4.4. Testing the two mixing techniques

To test the mixing approaches, experiments were run to assess how accurately each technique determined ϕ. First, a series of artificial parent PDFs were created by combining the parent Greater and Lesser Himalayan samples in varying proportions. The artificially created PDFs had ϕ values of 0.09, 0.2, 0.25, 0.33, 0.5, 0.66, 0.75, 0.8, and 0.91. With no subsampling, both the inverse and iterative approaches calculated the correct ϕ value over the entire range of artificial mixtures. This demonstrates that when the two fundamental assumptions (see Section 5.3) are satisfied, the mixing ratio can be perfectly calculated by both techniques.

Because our field samples represent an imperfect approximation of the parent age distribution from which they were drawn, it is important to simulate how well each technique can determine ϕ using imperfectly subsampled PDFs, i.e., 100 ages randomly selected from the parent PDF. Using the artificial PDFs described above and the subsampling procedure described in Section 5.2, ϕ was determined for each of the subsampled artificial PDFs. To determine the average accuracy and precision of each technique, 100 trials were performed and the results were averaged for each artificial ϕ. Over 100 trials, moderate ϕ values, ranging from 0.25 to 0.75 were accurately estimated, whereas more extreme ϕ values (0.09 to 0.2 and .8 to 0.91) were misestimated by 0.01–0.03. For each ϕ value, the standard deviation of 100 trials was around 0.05. These data suggest that: (1) extreme ϕ values are not accurately determined without smoothing; and (2) regardless of accuracy, the absolute 1σ error on any unsmoothed mixing estimate is ± 0.05.

Given the contrasting complexity of the Lesser and Greater Himalayan PDFs, we attempted to determine the combination of smoothing that would provide the most accurate mixing calculation for our field samples. Subsampled PDFs were again created from the artificial parents A, B and C. Each PDF was smoothed with successively larger windows between 0 and 100 My in increments of 10 My. Next, mixing calculations were performed for every possible combination of smoothed subsamples A, B and C. The results can be envisioned as a three-dimensional "smoothing matrix" on which each axis represents the degree of smoothing of one of the three PDFs (Fig. 7C). Each entry in the matrix represents the ϕ value calculated using a unique combination of the three smoothed PDFs. For each artificial ϕ value, 100 trials were performed and the 100 resulting matrices were combined, yielding an averaged smoothing matrix for each ϕ value. Each entry in the smoothing matrix was then subtracted from the expected ϕ value, resulting in a "difference matrix." This experiment identified the unique combination of smoothing that yielded the most accurate ϕ value with the lowest standard deviation over 100 trials.

Several interesting results emerged (Fig. 7A). For moderate ϕ values (0.25–0.75), increased smoothing of the mixed PDF C required increased smoothing of A and B to achieve an accurate calculation. Likewise, as previously observed, for moderate ϕ values the Greater Himalyan PDF consistently required 2–3 times more smoothing than the Lesser Himalayan PDF to achieve an accurate calculation. In contrast, for extreme ϕ values when the proportion of one component PDF (A or B) in C was less than 20%, the calculated mixing result was independent of how the smaller component was smoothed. For example, for a ϕ value of 0.09, any Greater Himalayan smoothing window produced an accurate result. Hence for moderate ϕ values, the complexity of the PDF determines how much smoothing is required, whereas for extreme ϕ values the optimal smoothing value is controlled by the dominant proportion of a constituent PDF (A or B) in the mixed PDF (C).

Because the mixing proportion of our field samples is unknown, but we would like to choose the smoothing combination that gives the most accurate mixing calculation, we chose to average the smoothing matrices for all ϕ values to create a single matrix displaying the optimal smoothing combination for the entire range of ϕ values (Fig. 7A). These results show that accurate mixing estimates can be achieved over a range of smoothing combinations.

5. 2-d multiple ratio mixing technique

Construction of an age PDF requires quasi-subjective decisions such as which type of age to use and

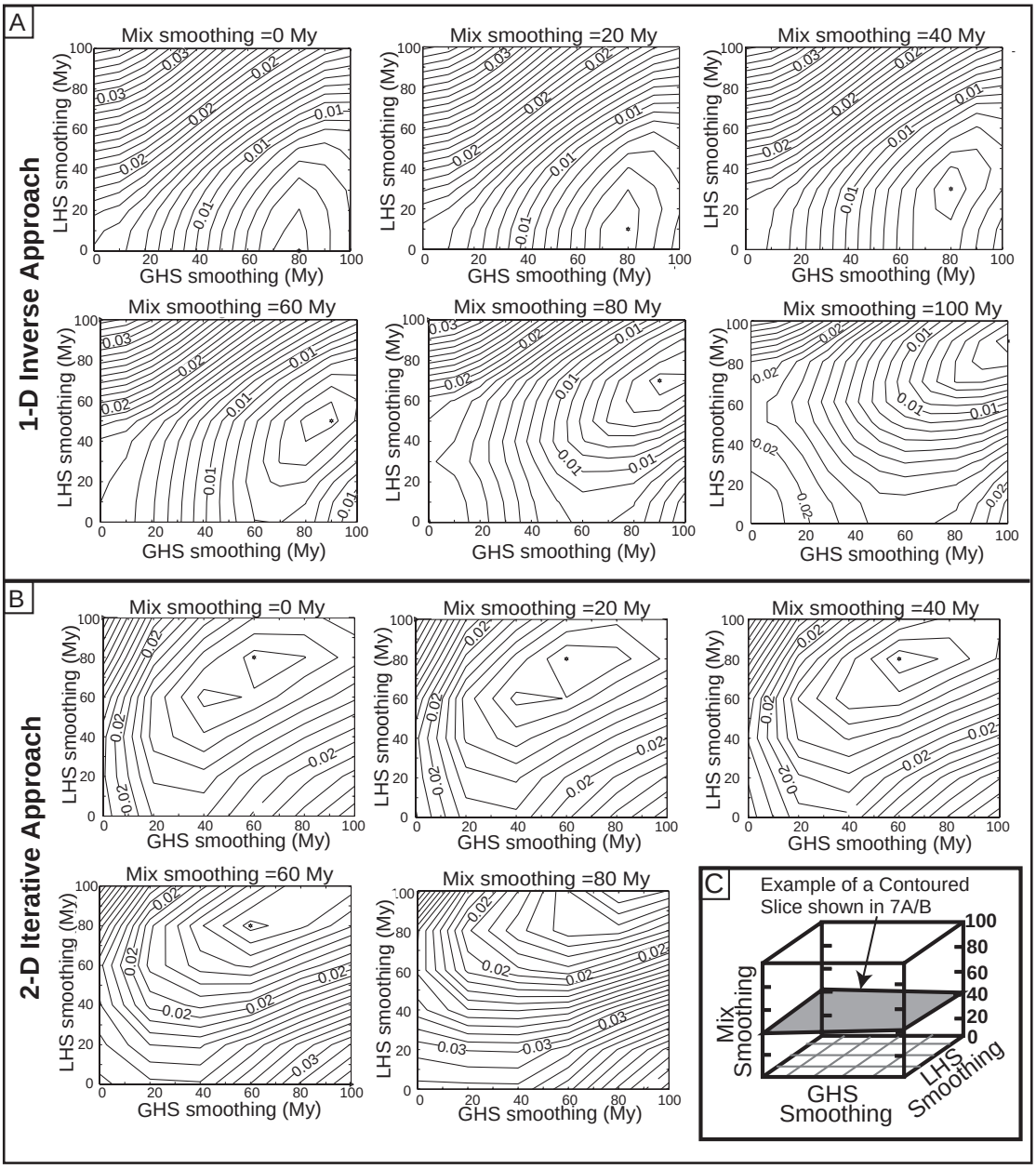

Fig. 7. The combination of PDF smoothing that yielded the most accurate mixing calculation was determined experimentally by: (1) creating subsampled PDFs ($n=100$) from the Greater Himalayan, Lesser Himalayan and the artificially mixed parent; (2) creating a smoothing "matrix" in which ϕ was calculated using every possible combination of smoothed PDFs; (3) repeating and averaging the smoothing matrices over 100 trials for each ϕ value; (4) subtracting each entry in the averaged smoothing matrix from the expected ϕ value to create a "difference matrix" for each ϕ value; (5) averaging the difference matrices for all ϕ values to determine which combination of smoothing yielded the most accurate mixing result over the entire range of ϕ values. (A) The averaged difference matrix for the 1-d inverse approach is shown in contoured slices through the "mix smoothing" axis. Notice that in all cases, the Greater Himalayan PDFs require more smoothing to achieve an accurate mixing result, but a minimum mismatch of ~0.003 can be achieved for a range of smoothing combinations. (B) The averaged difference matrix for the 2-d iterative approach is shown in contoured slices through the "mix smoothing" axis. (C) A cartoon diagram of a "difference matrix" illustrating the concept of contoured slices.

what selection criteria to use when discarding discordant ages. These decisions can have a profound effect on the resulting PDF. For example, a discordant zircon grain that has experienced a single episode of lead loss could have a $^{238}U/^{206}Pb$ age of 1 Gy, but a much older $^{207}Pb/^{206}Pb$ age reflecting its true crystallization age (see Fig. 2 online). Whereas traditional PDFs display only a single interpreted age for each grain, use of both the $^{238}U/^{206}Pb$ and $^{207}Pb/^{206}Pb$ ratios avoids subjectivity while providing additional criteria to differentiate single grains. In this section, we adapt our iterative and inverse mixing techniques to utilize both the $^{238}U/^{206}Pb$ and $^{207}Pb/^{206}Pb$ ratios to estimate zircon-grain mixing.

5.1. Constructing 2-d probability fields

The 2-d iterative approach is based on the inverse concordia diagram which plots each grain analysis using the $^{238}U/^{206}Pb$ ratio on the x-axis and the $^{207}Pb/^{206}Pb$ ratio on the y-axis. Within concordia space, each analysis is represented by an error ellipse defined by the Gaussian error around each ratio measurement. To perform the mixing calculation, the concordia space is converted into gridded field with equal increments on the x- and y-axes for all samples. Because each Gaussian error sums to 1, the two errors for a given analysis are cross multiplied to create a single probability grid for each analysis which sums to 1. The individual probability grids for multiple grains are then summed and normalized by the total number of grains to create a larger probability field that also sums to 1 (Fig. 8). The probability value of any grid cell represents the probability of drawing that unique ratio combination from the sample.

5.2. The 2-d iterative approach

The 2-d iterative approach determines ϕ by combining the probability fields for samples A and B in every possible combination until the resulting probability field $C_{\text{predicted}}$ has the lowest mismatch with C_{observed}. Again, the fundamental issue becomes which "mismatch" criteria should be iteratively minimized. Attempts were made to estimate ϕ by minimizing percent areal mismatch, sum of the squared differences between all cells, and the 2-D K–S statistic [34]. The sum of the squared differences proved to be the most effective mismatch criteria because the 2-D K–S statistic was not sensitive enough to small changes in ϕ, whereas the simple areal mismatch placed too much weight on cells with very small probabilities.

5.3. The 2-d inverse approach

The 2-d inverse approach begins by creating two sets of traditional PDFs for each sample, one created using measured $^{238}U/^{206}Pb$ ratios and another using measured $^{207}Pb/^{206}Pb$ ratios (not ages). We can now assume that either set of PDFs should satisfy the relationship described by Eq. (5). Assuming that the PDFs A, B, and C in Eq. (5) are constructed from $^{238}U/^{206}Pb$ ratios, we write a second equation expressing the same relationship for PDFs D, E, and F which are constructed from $^{207}Pb/^{206}Pb$ ratios:

$$[P(D) - P(E)]\phi = [P(F) - P(E)]. \quad (7)$$

Because all PDFs are constructed with the same x-axis intervals, we can then combine the linear Eqs. (5) and (7) yielding a combined equation of the form $Ax = B$:

$$[P(A) - P(B) - P(D) + P(E)]\phi = [P(C) - P(B) - P(F) + P(E)]. \quad (8)$$

Again, A and B are column vectors with a single row entry for each age increment (i), while ϕ is the unique mixing parameter that best satisfies the equality at every age increment (i). The least-squares estimate of ϕ can be attained as described in Section 4.3.1.

5.4. Testing the multiple ratio approaches

A series of experiments similar to those described for the 1-d mixing techniques (Section 5.4) were performed to evaluate the effectiveness of the multiple ratio approaches. Using the same ϕ values, a series of artificial ratio distributions were created. Without any subsampling, both the 2-d approaches perfectly estimated the artificial ϕ values over the entire range. Repeating the experiment using 100 subsampled ratio pairs showed that, averaged over 100 trials, the two techniques accurately predicted ϕ

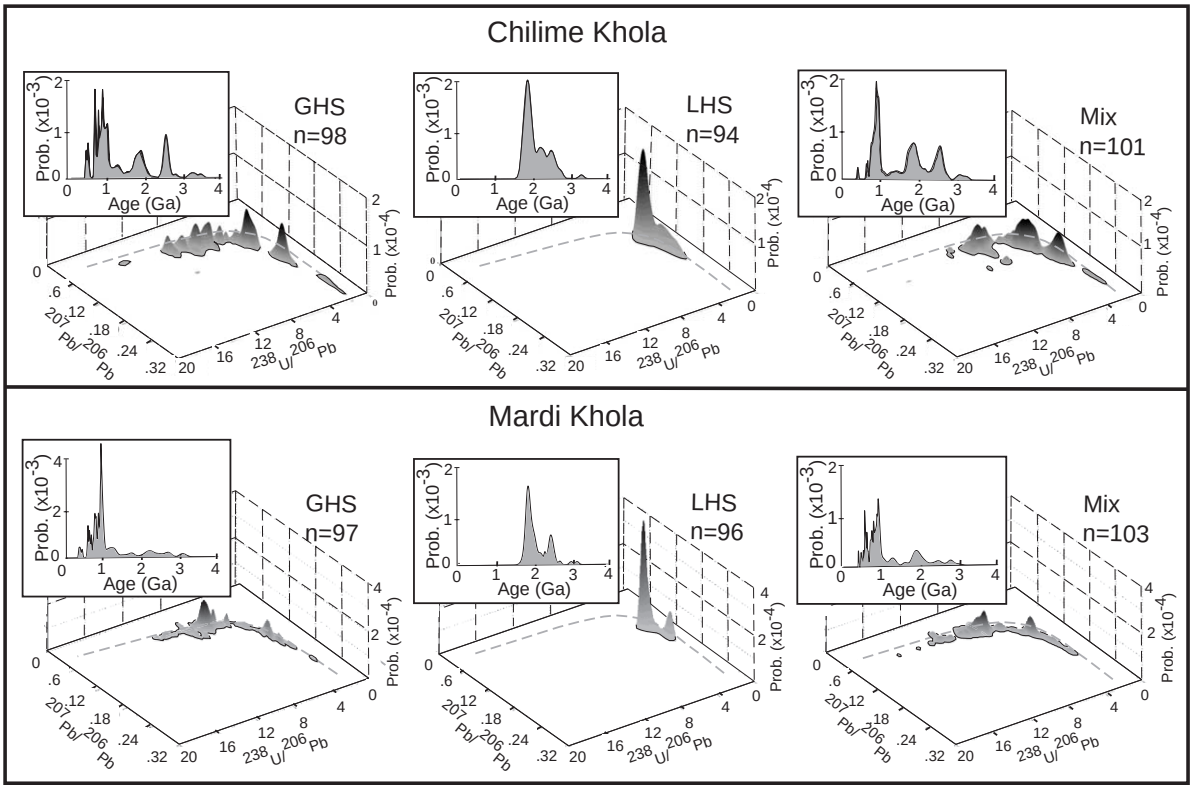

Fig. 8. Probability distributions for zircon samples from the Chilime Khola and Mardi Khola used to calculate relative erosion rates. Traditional age PDFs (inset boxes) are constructed from interpreted $^{238}U/^{206}Pb$ and $^{207}Pb/^{206}Pb$ ages and 2-d probability fields are constructed from measured $^{238}U/^{206}Pb$ and $^{207}Pb/^{206}Pb$ ratios, as described in the text. Results of the mixing calculation are presented in the text and displayed in Table 2 online.

values ranging from 0.3 to 0.6, but underestimated more extreme ϕ values. Regardless of ϕ value, the 2-d iterative approach showed a 1σ error of around 0.06, while the 2-d inverse approach had a 1σ error around 0.07.

To determine what combination of smoothing would provide the most accurate mixing calculation for our field samples, we again created smoothing matrices for each artificial ϕ value (Section 5.4) in which subsampled probability fields were smoothed in increments of 20 My, from 0 to 100 My. Averaged smoothing and difference matrices were created from 100 trials for each artificial ϕ value. Finally, the difference matrices for each ϕ value were averaged into a single matrix representing the full range of ϕ values (Fig. 7B).

Results show that highly accurate estimates of ϕ can be obtained over the entire range of ϕ values, but that the optimal smoothing combination is highly variable for different ϕ values. As a result, the most accurate smoothing combination displayed in the averaged difference matrix is only accurate within ± 0.007. This optimal combination is achieved by smoothing the Greater Himalaya to ~60 My, Lesser Himalaya to ~80 My and the mix to ~40 My. In contrast to the 1-d approach, simpler distributions with few peaks require more smoothing than diffuse, multi-peaked distributions.

6. Himalayan relative erosion rates

We used all four mixing approaches (1-d and 2-d, iterative and inverse) to determine relative erosion rates between catchments above and below the MCT in central Nepal (Fig. 1). Based on the modeling

results, the Greater Himalayan, Lesser Himalayan and mixed PDFs were smoothed to 80, 30, and 10 My, respectively. Mixing values calculated using the multiple-ratio approaches used smoothing of 60, 80, and 40 My for the Greater Himalayan, Lesser Himalayan, and mixed samples, respectively. Results (see Table 2 online) from the four techniques produced very similar estimates of ϕ for each site (Mardi Khola: 0.87 to 0.89; CK: 0.8 to 0.82). These results indicate that 4- to 8-fold more zircons were being contributed from the Greater Himalayan catchments in comparison to the Lesser Himalayan catchments. Following Eq. (1), calculated zircon mixing ratios were corrected for up to 5-fold differences in zircon concentration and drainage area (see Table 1 online). In contrast to zircon mixing ratios, corrected results from both study drainages show that relative erosion rates are ~3-times greater in the northernmost Lesser Himalayan than in the adjacent Greater Himalaya (see Table 2 online).

7. Discussion

7.1. Assumptions and sources of error

Most of the assumptions in our technique arise from two basic assertions: (1) samples are representative of the average spatial and temporal sediment flux from a catchment; and (2) mixing of zircon ages is representative of bulk sediment mixing, which is a proxy for total erosional flux.

The first assertion requires assuming that sediments are well mixed through time and space, alluvial storage is insignificant, and that the sample is truly random. In rapidly eroding ranges, such as the Himalaya, these assumptions are typically valid because the high discharge and velocity during the monsoon create a turbulent system with rapidly mixed sediments and little storage. The supply-limited conditions of the drainages mean that a single landslide is unlikely to overwhelm the river's sediment transport capacity or cause sudden deposition of sediments from a single source region. This implies that the composition of a sediment sample represents the average year-round sediment flux, rather than a single depositional event.

The second assertion assumes that zircons are well mixed within the coarse sand fraction, and that mixing of the coarse sand fraction is representative of bulk sediment mixing. Due to their high density, zircons can become concentrated in placer deposits by hydraulic sorting. However, in the absence of intense sorting, zircons should be well mixed within a sediment load of lighter, similarly shaped grains 2–3 times as large. To ensure a well-mixed sample, we amalgamated 10–15 grab samples combined from different coarse sand deposits that showed the least evidence of hydraulic sorting at each site. The assumption that mixing of coarse sand is representative of bulk sediment mixing is intricately linked to the grain-size distribution in each of the drainages. Without a detailed grain-size analysis of each drainage, we must assume that both drainages have comparable grain-size distributions and that the coarse fraction is representative of the total erosional flux. The latter assumption is dependent upon the proportion of erosion that occurs by chemical weathering, which is thought to be negligible in the high Himalaya.

The error associated with the relative erosion rate estimate is derived primarily from the concentration and mixing estimates. Based on the good agreement between the estimated and counted grains/gram concentrations (Fig. 4), the error in grain frequency should be <10%. The modeling results suggest that the absolute 1σ error around a single 1-d mixing estimate is ± 0.05, and about ± 0.06 for a 2-d estimate. This error is primarily due to the inaccuracy in reproducing extremely complex PDFs with a100-grain subsample and future studies using simpler distributions or more grain ages should easily achieve lower errors. It is also possible to calculate the error on any single estimate of ϕ based on the covariance of the inversion, although this calculation may not represent the true error on the precision of ϕ. For example, if distributions A, B and C are misrepresented in such a way that an incorrect ϕ value happens to create a perfect fit for the inversion, then the error on the true value of ϕ will be higher than estimated based on the inversion alone.

In general, the 1- and 2-d techniques have achieved comparable results for both the experimental modeling and the mixing calculation using field data. Although neither technique shows a clear advantage in this study, this may reflect the fact that badly discordant analyses were eliminated prior to mixing calculations. The 2-d technique is likely to be more

useful when dealing with populations of badly discordant detrital zircons, because of the inherent difficulties in interpreting accurate crystallization ages from single-grain analyses.

7.2. Importance of estimating zircon concentration

Previous studies of mineral age mixing have commonly assumed that the mineral concentration was uniform between samples from different catchments [7]. Our methods for estimating zircon concentrations show that concentrations in river sediment can vary by at least 2–3-fold. Failure to incorporate this difference into mixing calculations would result in 2- and 5-fold underestimates for the Mardi Khola and Chilime Khola, respectively. Likewise, point counting of detrital micas in 15 samples from the central Himalaya showed 100-fold variations in their concentrations [36]. If the variations in the abundance of zircon and mica in the central Himalaya are typical of other regions, then reliable calculations of relative erosion rates or of contributions from tributary catchments require reliable estimates of mineral concentrations.

7.3. Implications of Himalayan erosion rates

This study suggests that modern erosion rates in the northernmost Lesser Himalaya are ~3-times higher than in the Greater Himalaya. This result disagrees with the hypothesis that recent rock uplift along the MCT is driving rapid erosion primarily within the Greater Himalaya. Also, it apparently contradicts estimates based on apatite fission-track dating that suggest mean Quaternary rates as much as an order-of-magnitude higher in the Greater Himalaya on 10^5–10^6 yr timescales [30]. Instead, at face value, this result suggests more rapid erosion of the northernmost Lesser Himalaya. This result suggests that if modern erosion rate is driven by rock-uplift rate, then the focus of recent deformation is south of the MCT near the PT_2. Similarly, if deformation is distributed 1–2 km south of the MCT, increased fracturing and weakening of rocks might contribute to more rapid rates of erosion throughout this zone.

The fact that higher erosion rates are spatially coincident with the peak in monsoonal precipitation [30] is also consistent with the idea that focused precipitation is driving rapid erosion rates near the range front [10]. However, this interpretation is paradoxical in that our modern erosion rates agree with inferences based on long-term ($^{40}Ar/^{39}Ar$) rates [9] whereas they disagree with intermediate-term Quaternary rates (apatite fission-track) [30]. The apparent disconnect between modern and Quaternary rates might be explained by short-term climate variability which is currently driving focused erosion in the uppermost Lesser Himalaya, but is overwhelmed by a spatially consistent tectonic signal or glacial erosion in the Greater Himalaya on Quaternary timescales. This explanation would imply that the correlation between the peak in modern precipitation and the break in long-term exhumation rates is a coincidence, and is perhaps driven by other factors such as the existence of a crustal-scale ramp along the basal Himalayan detachment fault or "extrusion" of the northern Lesser Himalaya associated with relative down-to-the-north extension of the Greater Himalaya [27,28,31].

Another possible explanation for the disagreement between erosion rates on three different timescales is that the exhumational regime has been unsteady since the late Miocene. This idea is supported by the combination of apatite fission-track and muscovite $^{40}Ar/^{39}Ar$ ages south of the PT_2 (Fig. 3). Even if the thermal gradient over the last 4 My was compressed to ~70 °C/km, the AFT ages would correspond to <2 km of exhumation at a rate of >0.5 km/My. In contrast, if a gentle gradient of 12 °C/km is assumed for the last 800 My, then the $^{40}Ar/^{39}Ar$ ages correspond to ~30 km of exhumation at a rate of ~0.038 km/My. Thus, thermochronologic evidence suggests that exhumation rates in the Lesser Himalaya have increased by at least an order of magnitude in the last 4 My in response to major changes in the tectonic and/or climatic forcing regime. Such changes suggest that exhumational steady state [37] in the Himalaya is unlikely at timescales of more than a few million years.

8. Conclusions

This paper presents new mixing techniques to deconvolve the relative proportion of U–Pb zircon ages contributed from two known sources to a finite mixture. Both the 1-d and 2-d mixing techniques accu-

rately estimate mixing between zircon populations if: (1) the resulting mixture is a finite combination; and (2) all mixing components are perfectly known. Because these assumptions are rarely met, some degree of sample smoothing is usually required to achieve an accurate mixing calculation. This study achieved estimates of the mixing parameter ϕ accurate to within ± 0.05, with potentially higher accuracy attainable in systems with simpler age distributions.

The two mixing techniques were used to calculate relative erosion rates between adjacent drainage basins in the Nepal Himalaya. To assume that zircon mixing is representative of sediment mixing and erosion rates, corrections for zircon concentration and drainage area must be applied. We use both zircon-grain counting and XRF analysis of bulk Zr to estimate zircon concentration, thus providing a cross-check on the accuracy of both techniques. The resulting 2–3-fold difference in zircon concentration between drainages reveals the largely unrecognized importance of mineral concentration in detrital mineral studies.

Results suggest that modern erosion rates are ~3 times higher in the northernmost parts of the Lesser Himalaya than in the adjacent Greater Himalaya. Accordingly, higher rates of rock uplift north of the MCT do not appear to be driving modern erosion rates. Instead, accelerated modern erosion rates in the northern Lesser Himalaya are consistent with the concept of active deformation localized south of the MCT and correspond spatially with the peak in monsoonal precipitation. These preliminary conclusions might be tested by additional estimates of relative erosion rates based on mixing of Nd isotopes or by cosmogenic dating of bulk sediments.

The techniques developed in this study have strong potential for applications in the fields of geomorphology, sedimentology, and paleotectonics. Tracing individual populations of sediment through the fluvial system has important implications for the study of sediment transport and deposition on the reach scale. Quantitative resolution of the relative amounts of sediment in a closed sedimentary basin derived from known source terranes has potential for improved understanding of sedimentary process and tectonic reconstructions. Finally, improved understanding of the behavior of heavy minerals in orogen-scale drainage systems could improve interpretation of mineral cooling ages in foreland sediments.

Acknowledgments

We thank Luc Mehl, Nathan Niemi, Gabriel Rotberg, Michael Oskin, Beth Pratt-Sitaula, Dan Schmidt, Jenny Jones, and the Hacker Lab for their insight and assistance. We thank Drs. M. Bickle and K. Farley for insightful reviews of the manuscript. Support for this research was received from NSF Continental Dynamics [EAR 9909647]. Logistical arrangements were provided by Himalayan Experience.

Appendix A. Supplementary Data

Supplementary data associated with this article can be found, in the online version, at doi:10.1016/j.epsl.2005.03.019.

References

[1] A.C. Morton, C.R. Hallsworth, Processes controlling the composition of heavy mineral assemblages in sandstones, Sediment. Geol. 124 (1999) 3–29.
[2] L. Van der Plas, A.C. Tobi, A chart for judging the reliability of point counting results, Science 263 (1965) 87–90.
[3] P.D. Clift, J.I. Lee, P. Hildebrand, N. Shimizu, G.D. Layne, J. Blusztajn, J.D. Blum, E. Garzanti, A.A. Khan, Nd and Pb isotope variability in the Indus River System: implications for sediment provenance and crustal heterogeneity in the Western Himalaya, Earth Planet. Sci. Lett. 200 (2002) 91–106.
[4] A. Galy, C. France-Lanord, Higher erosion rates in the Himalaya; geochemical constraints on riverine fluxes, Geology 29 (1) (2001) 23–26.
[5] M.T. Brandon, Decomposition of fission-track grain-age distributions, Am. J. Sci. 292 (1992) 535–564.
[6] M.S. Sambridge, W. Compston, Mixture modeling of multi component data sets with application to ion-probe zircon ages, Earth Planet. Sci. Lett. 128 (1994) 373–390.
[7] M. Bernet, M.T. Brandon, J.I. Garver, B. Moliter, Downstream changes of Alpine zircon fission-track ages in the Rhone and Rhine rivers, J. Sediment. Res. 74 (1) (2004) 82–94.
[8] P.M. Myrow, N.C. Hughes, T.S. Paulsen, I.S. Williams, S.K. Parcha, K.R. Thompson, S. Bowring, S.C. Peng, Ahluwalia, Integrated tectonostratigraphic analysis of the Himalaya and implications for its tectonic reconstruction, Earth Planet. Sci. Lett. 212 (2003) 433–441.
[9] C. Wobus, K.V. Hodges, K.X. Whipple, Has focused denudation sustained active thrusting at the Himalayan topographic front, Geology 31 (10) (2003) 861–864.
[10] K.V. Hodges, C. Wobus, K. Ruhl, T. Schildgen, K.X. Whipple, Quaternary deformation, river steepening and heavy precipita-

tion at the front of the Higher Himalayan ranges, Earth Planet. Sci. Lett. 220 (3–4) (2004) 379–389.
[11] J. Lave, J.P. Avouac, Fluvial incision and tectonic uplift across the Himalayas of central Nepal, J. Geophys. Res., B 106 (11) (2001) 26561–26591.
[12] P.G. Decelles, D.M. Robinson, J. Quade, T.P. Ojha, C.N. Garzione, P. Copeland, B.N. Upreti, Stratigraphy, structure and tectonic evolution of the Himalayan fold and thrust belt in western Nepal, Tectonics 20 (4) (2001) 487–509.
[13] D.M. Robinson, P.G. Decelles, P.J. Patchett, C.N. Garzione, The kinematic evolution of the Nepalese Himalaya interpreted from Nd isotopes, Earth Planet. Sci. Lett. 192 (4) (2001) 507–521.
[14] P. Copeland, M. Harrison, K.V. Hodges, P. Maruejol, P. Le Fort, A. Pecher, An early Pliocene thermal disturbance of the main central thrust, central Nepal: implications for Himalayan tectonics, J. Geophys. Res. 96 (B5) (1991) 8475–8500.
[15] P. Le Fort, Himalayas; the collided range; present knowledge of the continental arc, Am. J. Sci. 275A (1975) 1–44.
[16] G.E. Gehrels, P.G. Decelles, A. Martin, T.P. Ojha, G. Pinhassi, Initiation of the Himalayan Orogen as an Early Paleozoic Thin-skinned Thrust Belt, GSA Today 13 (9) (2003) 4–9.
[17] A. Martin, P.G. Decelles, G.E. Gehrels, P.J. Patchett, C. Isachsen, Isotopic and microstructural constraints on the location of the main central thrust in central Nepal Himalaya, Geol. Soc. Am. Bull. in press.
[18] D.M. Robinson, P.G. Decelles, C.N. Garzione, O. Pearson, M. Harrison, E.J. Catlos, Kinematic model for the main central thrust in Nepal, Geology 31 (31) (2003) 359–362.
[19] A.J. Meigs, D.W. Burbank, R.A. Beck, Middle-late Miocene (>10 Ma) formation of the Main Boundary Thrust in the western Himalaya, Geology 23 (5) (1995) 423–426.
[20] K.V. Hodges, Tectonics of the Himalaya and Southern Tibet from two perspectives, Geol. Soc. Am. Bull. 112 (2000) 324–350.
[21] C. Wang, Z. Liu, H. Yi, S. Liu, X. Zhao, Tertiary crustal shortening and peneplanation in the Hoh Xil region; implications for the tectonic history of the Northern Tibetan Plateau, J. Asian Earth Sci. 20 (3) (2002) 211–223.
[22] J. Lave, J.P. Avouac, Active folding of fluvial terraces across the Siwalik Hills, Himalayas of central Nepal, J. Geophys. Res. 105 (B3) (2000) 5735–5770.
[23] M. Jackson, R. Bilham, Constraints on Himalayan deformation inferred from vertical velocity fields in Nepal and Tibet, J. Geophys. Res., B 99 (7) (1994) 13897–13912.
[24] L. Seeber, V. Gornitz, River profiles along the Himalayan arc as indicators of active tectonics, Tectonophysics 92 (1983) 335–367.
[25] B. Pratt-Sitaula, D.W. Burbank, A. Heimsath, T.P. Ojha, Landscape disequilibrium on 1000–10,000 year scales Marsyandi River, Nepal, central Himalaya, Geomorphology 58 (2004) 223–241.
[26] E. Gabet, B. Pratt-Sitaula, D.W. Burbank, Climatic controls on hillslope angle and relief in the Himalayas, Geology 32 (7) (2004) 629–632.
[27] K.V. Hodges, J.M. Hurtado, K.X. Whipple, Southward extrusion of Tibetan crust and its effect on Himalayan tectonics, Tectonics 20 (6) (2001) 799–809.
[28] R. Caittin, J.P. Avouac, Modeling mountain building and the seismic cycle in the Himalayas of Nepal, J. Geophys. Res. 106 (B8) (2000) 13389–13407.
[29] E.J. Catlos, T.M. Harrison, M.J. Kohn, M. Grove, F.J. Ryerson, C. Manning, B.N. Upreti, Geochronologic and thermobarometric constraints on the evolution of the Main central Thrust, central Nepal Himalaya, J. Geophys. Res., B 106 (8) (2001) 16177–16204.
[30] D.W. Burbank, A.E. Blythe, J. Putkonen, B. Pratt-Sitaula, E. Gabet, M. Oskin, A. Barros, T.P. Ojha, Decoupling of erosion and precipitation in the Himalaya, Nature 426 (2003) 652–655.
[31] C. Beaumont, R.A. Jamieson, M.H. Nguyen, B. Lee, Himalayan tectonics explained by extrusion of a low viscosity crustal channel coupled to focused surface denudation, Nature 414 (2001) 738–742.
[32] S.D. Willett, Orogeny, orography; the effects of erosion on the structure of mountain belts, J. Geophys. Res. 104B (12) (1999) 28957–28982.
[33] W.R. Dickinson, G.E. Gehrels, U–Pb ages of detrital zircons from Permian and Jurassic eolian sandstones of the Colorado Plateau, USA: paleogeographic implications, Sediment. Geol. 163 (2003) 29–66.
[34] W.H. Press, Numerical Recipes in C: the Art of Scientific Computing, Cambridge University Press, Cambridge, 1997, 994 pp.
[35] W. Menke, Geophysical Data Analysis: Discrete Inverse Theory, Academic Press, San Diego, 1989, 289 pp.
[36] I.D. Brewer, Detrital–Mineral Thermochronology: Investigations of Orogenic Denudation in the Himalayas of Nepal, Pennsylvania State University, 2001.
[37] S.D. Willett, M.T. Brandon, On steady states in mountain belts, Geology 30 (2) (2002) 175–178.
[38] M.E. Coleman, K.V. Hodges, Contrasting Oligocene and Miocene thermal histories from the hanging wall and footwall of the South Tibetan detachment in the central Himalaya from 40Ar/39Ar thermochronology, Marsyandi Valley, central Nepal, Tectonics 17 (5) (1998) 726–740.
[39] M. Colchen, P. Le Fort, A. Pecher, Geological Researches in the Nepal Himalaya, Annapurna–Manaslu–Ganesh Himal; Notice of the Geological Map on 1/200,000, Centre National de la Recherche Scientifique, Paris, 1986.
[40] A.M. MacFarlane, K.V. Hodges, D. Lux, A structural analysis of the main central Thrust zone, Langtang national park, central Nepal Himalaya, Geol. Soc. Am. Bull. 104 (1992) 1389–1402.
[41] A.M. MacFarlane, Chronology of tectonic events in the crystalline core of the Himalaya, Lantang National Park, central Nepal, Tectonics 12 (4) (1993) 1004–1025.